Simultaneous Transitions in Cuprate Momentum-Space Topology and Electronic Symmetry Breaking

Simultaneous Transitions in Cuprate Momentum-Space Topology and Electronic Symmetry Breaking

K. Fujita,[1,2,3]* Chung Koo Kim,[1]* Inhee Lee,[1] Jinho Lee,[1,4,5] M. H. Hamidian,[1,2] I. A. Firmo,[2] S. Mukhopadhyay,[2,6] H. Eisaki,[7] S. Uchida,[3] M. J. Lawler,[2,8] E.-A. Kim,[2] J. C. Davis[1,2,9,10]†

The existence of electronic symmetry breaking in the underdoped cuprates and its disappearance with increased hole density p are now widely reported. However, the relation between this transition and the momentum-space ($\vec{\mathbf{k}}$-space) electronic structure underpinning the superconductivity has not yet been established. Here, we visualize the $\vec{\mathbf{Q}} = 0$ (intra–unit-cell) and $\vec{\mathbf{Q}} \neq 0$ (density-wave) broken-symmetry states, simultaneously with the coherent $\vec{\mathbf{k}}$-space topology, for $Bi_2Sr_2CaCu_2O_{8+\delta}$ samples spanning the phase diagram $0.06 \leq p \leq 0.23$. We show that the electronic symmetry-breaking tendencies weaken with increasing p and disappear close to a critical doping $p_c = 0.19$. Concomitantly, the coherent $\vec{\mathbf{k}}$-space topology undergoes an abrupt transition, from arcs to closed contours, at the same p_c. These data reveal that the $\vec{\mathbf{k}}$-space topology transformation in cuprates is linked intimately with the disappearance of the electronic symmetry breaking at a concealed critical point.

The highest known superconducting critical temperature T_c (1–3) occurs atop the $T_c(p)$ (where p is hole density) "dome" of hole-doped cuprates (Fig. 1A). In addition to the superconductivity, electronic broken-symmetry states (4) have also been reported at low p in many such compounds. Wave vector $\vec{\mathbf{Q}} = 0$ (intra–unit-cell) symmetry breaking, typically of 90°-rotational (C_4) symmetry, is reported in $YBa_2Cu_3O_{6+\delta}$, $Bi_2Sr_2CaCu_2O_{8+\delta}$, and $HgBa_2CuO_{4+x}$ (5–14). Finite wave vector $\vec{\mathbf{Q}} \neq 0$ (density-wave) modulations breaking translational symmetry, long detected in underdoped $La_{2-x-y}Nd_ySr_xCuO_4$ and $La_{2-x}Ba_xCuO_4$ (15, 16), are now also reported in underdoped $YBa_2Cu_3O_{7-\delta}$, $Bi_2Sr_2CuO_{6+\delta}$,

and $Bi_2Sr_2CaCu_2O_{8+\delta}$ (17–25). Summarizing all such reports in Fig. 1A reveals some stimulating observations. First, although the $\vec{\mathbf{Q}} = 0$ and $\vec{\mathbf{Q}} \neq 0$ states are detected by widely disparate techniques and are distinct in terms of symmetry, they seem to follow approximately the same phase-diagram trajectory (shaded band Fig. 1A), as if facets of a single phenomenon (26). The second implication is that a critical point (perhaps a quantum critical point) associated with these broken-symmetry states may be concealed beneath the $T_c(p)$ dome. Numerous earlier studies reported sudden alterations in many electronic and magnetic characteristics near $p = 0.19$ (2, 3, 27), but whether

these phenomena are caused by electronic symmetry changes (28) at a critical point was unknown.

In momentum space ($\vec{\mathbf{k}}$-space), the hole-doped cuprates also exhibit an unexplained transition in electronic structure with increasing hole density. Open contours, or "Fermi arcs" (29–32), are reported at low p in all compounds studied, whereas at high p closed holelike pockets surrounding $\vec{\mathbf{k}} = (\pm 1, \pm 1)\pi/a_0$ (where a_0 is the unit cell dimension) are observed (33, 34). One possibility is that such a transition could occur due to the disappearance of an electronic ordered state, with the resulting modifications to the Brillouin zone geometry altering the topology of the electronic bands (28).

Our strategy, therefore, is a simultaneous examination of both the $\vec{\mathbf{k}}$-space electronic structure and the $\vec{\mathbf{Q}} = 0$ and $\vec{\mathbf{Q}} \neq 0$ broken-symmetry states, over a sufficiently wide range of p to include any concealed critical point. The objective is to search for a relation between the broken-symmetry
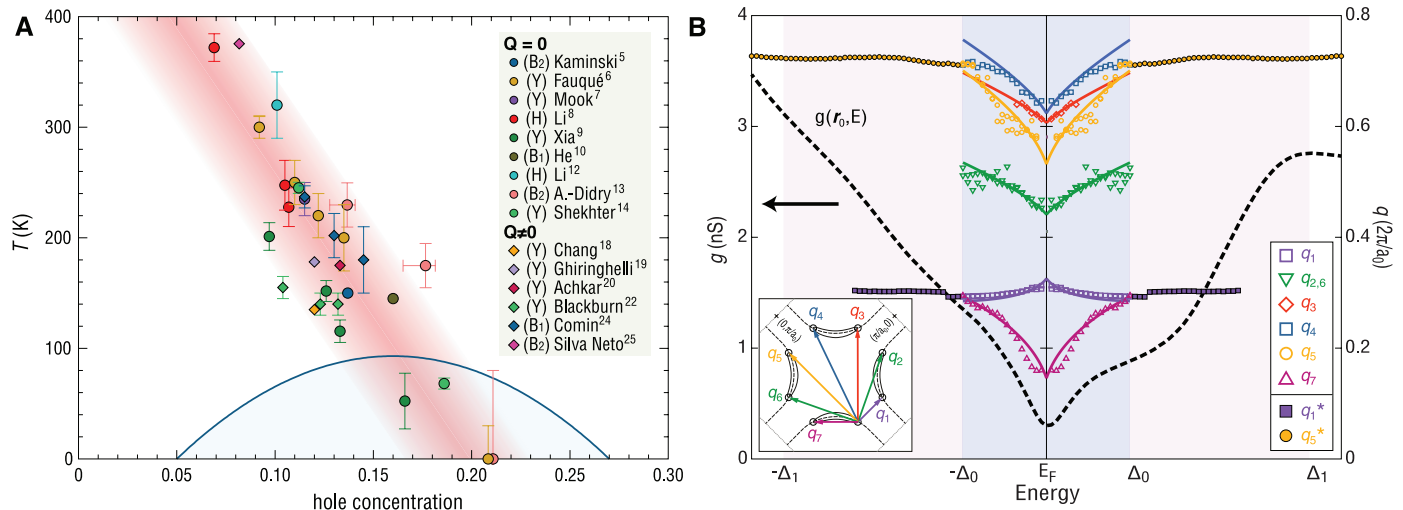
Fig. 1. Hole-density dependence of cuprate broken-symmetry states. (**A**) Phase diagram of hole-doped cuprates showing the $T_c(p)$ "dome" (blue curve). Symbols denote the onset temperature (T) of two types of symmetry breaking reported in $Bi_2Sr_2CuO_{6+\delta}$(B_1), $Bi_2Sr_2CaCu_2O_{8+\delta}$($B_2$), $YBa_2Cu_3O_{7-\delta}$(Y), and $HgBa_2CuO_{4+x}$(H). Circles, $\vec{\mathbf{Q}} = 0$ (intra–unit-cell) symmetry breaking; diamonds, $\vec{\mathbf{Q}} \neq 0$ broken translational symmetry (density waves). Error bars indicate the uncertainties in estimated hole concentration (horizontal) and the onset tem-

peratures (vertical). (**B**) The dashed black curve denotes the typical differential conductance spectrum $g(E)$ of underdoped $Bi_2Sr_2CaCu_2O_{8+\delta}$ here at $p = 0.06$. The pale blue shaded region indicates where the dispersive $\vec{\mathbf{q}}_m$ (E); $m = 1, 2, …, 7$ Bogoliubov QPI wave vectors indicative of Cooper pair breaking exist (color coded in inset); they disappear at energy Δ_0. Solid curves, simulation for QPI in a $d_{x^2-y^2}$ symmetry superconductor; pink shaded regions, quasi-static conductance modulations (density waves) exhibiting wave vectors $\vec{\mathbf{q}}_1^*$ and $\vec{\mathbf{q}}_5^*$.

states (5–25) and the Fermi surface (FS) topology (29–34). Fourier transform analysis of spectroscopic imaging scanning tunneling microscopy (SI-STM) is distinctive in that it allows access simultaneously to the $\vec{Q} = 0$ and $\vec{Q} \neq 0$ broken-symmetry states (26, 35) and to the $\vec{k}$-space electronic structure by using quasi-particle scattering interference (QPI) (35). The SI-STM tip-sample differential tunneling conductance $g(\vec{r}, E = eV)$ (e, electron charge; V, tip-sample bias voltage) at location $\vec{r}$ and energy E relates to density of electronic states $N(\vec{r}, E)$ as

$$g(\vec{r}, E) \propto \left[eI_S / \int_0^{eV_S} N(\vec{r}, E') dE' \right] N(\vec{r}, E) \ (I_S \text{ and}$$

V_S are arbitrary parameters) (35). In cuprates, it is necessary to study the ratio of the differential conductances $Z(\vec{r}, |E|) = g(\vec{r}, E)/g(\vec{r}, -E)$ because it suppresses the severe systematic errors due to the unknown denominator $\int_0^{eV_S} N(\vec{r}, E') dE'$ by division, thereby allowing $\vec{q}$-vectors and symmetries to be measured correctly (35).

The $\vec{k}$-space structure of coherent Bogoliubov quasi-particles is then detectable, because scattering between the eight density-of-states maxima at $\vec{k}_j(E)$; j = 1, 2, ...,8 (circles in inset Fig. 1B) produces interference patterns with wave vectors $\vec{q}(E) = \vec{k}_j(E) - \vec{k}_i(E)$ in $Z(\vec{q}, E)$, the Fourier transform of $Z(\vec{r}, E)$. At low p, one finds that the predicted set of seven inequivalent Bogoliubov

QPI wave vectors $\vec{q}_m(E)$; m = 1, 2, ...,7 (inset Fig. 1B) exist only below an energy Δ_0 (Fig. 1B), indicating that it is the limiting binding energy of a Cooper pair (35). At $|E| > \Delta_0$, the dispersive $\vec{q}_m$ disappear (Fig. 1B and movie S1) and are replaced by broken-symmetry states consisting of (i) spatial modulations with energetically quasi-static wave vectors $\vec{q}_1^*$ and $\vec{q}_5^*$ breaking translational symmetry (24, 25, 35, 36) and (ii) $\vec{Q} = 0$ (intra–unit-cell) breaking of C_4 symmetry detectable either directly in $\vec{r}$-space (11, 36) or at the Bragg wave vectors (11, 26, 35). But the complete doping dependence of these broken-symmetry signatures was unknown.

To determine the $\vec{k}$-space topology of coherent states across the phase diagram of $Bi_2Sr_2CaCu_2O_{8+\delta}$, we use a recently developed approach (37) that requires measurement of only a single QPI wave vector, $\vec{q}_4$ (blue arrow in Fig. 1B, inset). Brillouin zone geometry (Fig. 2A) means that $\vec{q}_4$ is simply related to the FS states $\vec{k}_F$ as
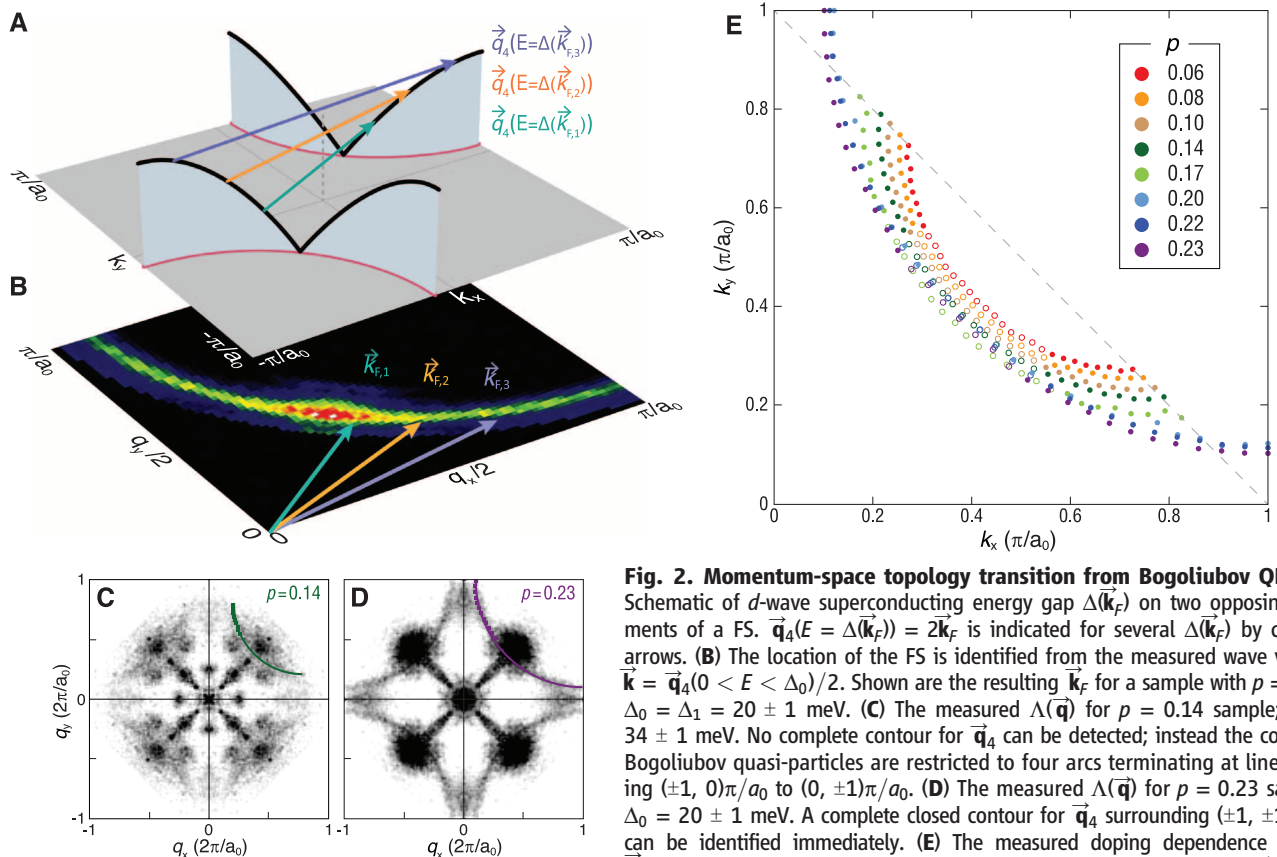
$$\vec{q}_4(E = \Delta(\vec{k}_F)) = 2\vec{k}_F \quad (1)$$

Here $\Delta(\vec{k})$ is the $d_{x^2-y^2}$ superconducting energy gap whose energy-minimum follows the trajectory of $\vec{k}_F$. An image of the locations of $\vec{q}_4(E)/2$ for all $0 < |E| < \Delta_0$ (pale blue region in Fig. 1B) then yields the FS location of coherent states that contribute to Cooper pairing. An efficient way to

locate these states is to sum all the $Z(\vec{q}, E)$ images to the energy Δ_0

$$\Lambda(\vec{q}) = \sum_{E \cong 0}^{\Delta_0} Z(\vec{q}, E) \quad (2)$$

and then to plot the contour of $\vec{q}_4$ within these $\Lambda(\vec{q})$ images (see supplementary text section I and figs. S1 and S2) (38). The power of this procedure is demonstrated in the determination of the FS in Fig. 2B (supplementary text section II) (38). Applying this $\Lambda(\vec{q})$ approach to determine the doping dependence of $\vec{k}$-space topology, we find very different results at low and high p. Figure 2C shows $\Lambda(\vec{q})$ at p = 0.14, whereas Fig. 2D shows $\Lambda(\vec{q})$ at p = 0.23. The most prominent difference between the two is that the contour of $\vec{q}_4$ only spans four arcs in Fig. 2C, whereas it completes four closed curves surrounding $\vec{q} = (\pm 1, \pm 1)2\pi/a_0$ in Fig. 2D. He et al. report similar phenomena in $Bi_2Sr_2CuO_{6+\delta}$ (37). In Fig. 2E, we show the complete doping dependence of measured $\vec{q}_4/2$ over the full range of p (supplementary text section II) (38). A notable transition in $\vec{k}$-space topology is observed within the narrow range $p \approx 0.19 \pm 0.01$, wherein the arc of coherent Bogoliubov states typical of low p suddenly switches to the complete closed contour surrounding $\vec{k} = (\pm 1, \pm 1)\pi/a_0$ (supplementary text section II, fig. S3, and movie S2) (38).

Fig. 2. Momentum-space topology transition from Bogoliubov QPI. (A) Schematic of d-wave superconducting energy gap $\Delta(\vec{k}_F)$ on two opposing segments of a FS. $\vec{q}_4(E = \Delta(\vec{k}_F)) = 2\vec{k}_F$ is indicated for several $\Delta(\vec{k}_F)$ by colored arrows. **(B)** The location of the FS is identified from the measured wave vectors $\vec{k} = \vec{q}_4(0 < E < \Delta_0)/2$. Shown are the resulting $\vec{k}_F$ for a sample with p = 0.23; $\Delta_0 = \Delta_1 = 20 \pm 1$ meV. **(C)** The measured $\Lambda(\vec{q})$ for p = 0.14 sample; $\Delta_0 = 34 \pm 1$ meV. No complete contour for $\vec{q}_4$ can be detected; instead the coherent Bogoliubov quasi-particles are restricted to four arcs terminating at lines joining $(\pm 1, 0)\pi/a_0$ to $(0, \pm 1)\pi/a_0$. **(D)** The measured $\Lambda(\vec{q})$ for p = 0.23 sample; $\Delta_0 = 20 \pm 1$ meV. A complete closed contour for $\vec{q}_4$ surrounding $(\pm 1, \pm 1)\pi/a_0$ can be identified immediately. **(E)** The measured doping dependence of the $\vec{k}$-space topology of coherent Bogoliubov quasi-particles using the $\vec{q}_4$ technique. The transition from arcs terminating at the lines $(\pm 1, 0)\pi/a_0$ to $(0, \pm 1)\pi/a_0$ to complete hole-pockets surrounding $(\pm 1, \pm 1)\pi/a_0$ at $p \approx 0.19$ is evident.
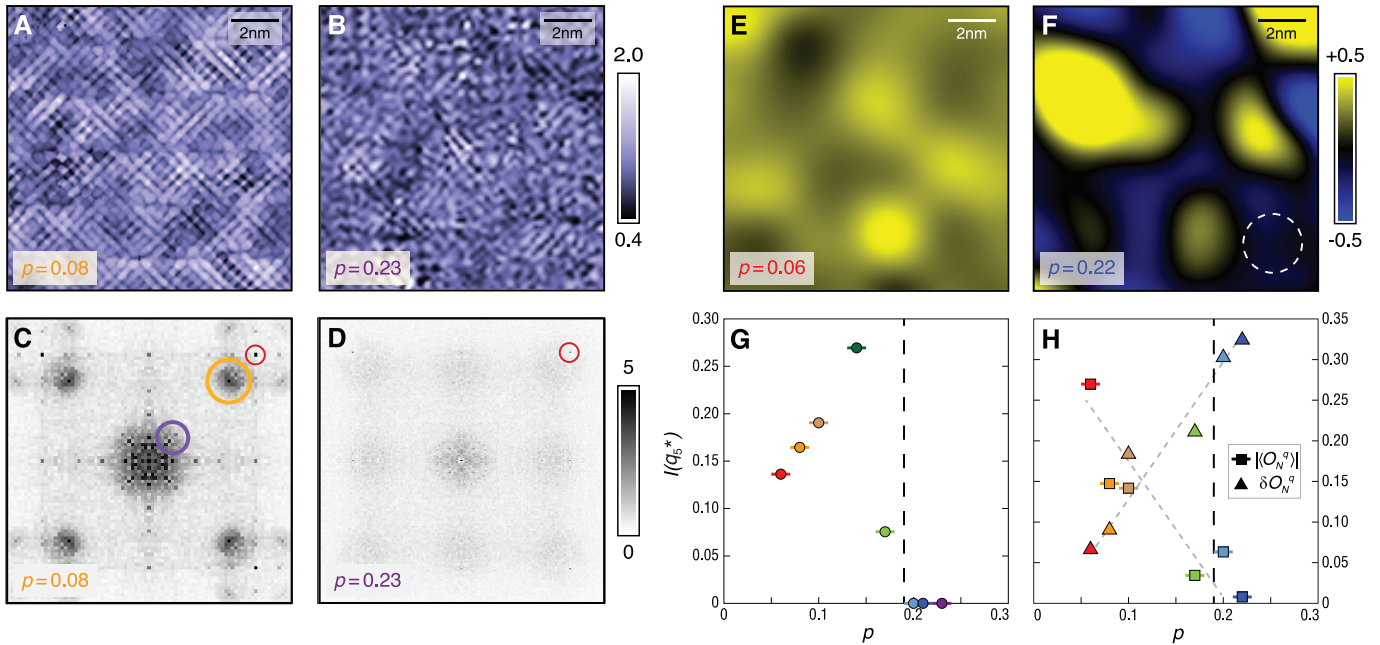
Fig. 3. Measurements of hole-density dependence of $\vec{\mathbf{Q}} = 0$ and $\vec{\mathbf{Q}} \neq 0$ ordering. (**A**) $Z(\vec{\mathbf{r}}, E \sim \Delta_1)$ for $p = 0.08$. Incommensurate conductance modulations are clearly seen; $\Delta_1 = 84 \pm 1$ meV. (**B**) $Z(\vec{\mathbf{r}}, E \sim \Delta_1)$ for $p = 0.23$ is shown; $\Delta_1 = 20 \pm 1$ meV. No specific $\vec{\mathbf{q}}$-vector for modulations is seen, although the QPI signature of Bogoliubov quasi-particles does produce a jumbled standing wave pattern. (**C**) $Z(\vec{\mathbf{q}}, E \sim \Delta_1)$ for $p = 0.08$ from (A); $\vec{\mathbf{q}}_1^*$ and $\vec{\mathbf{q}}_5^*$ wave vectors are indicated by purple and orange circles, respectively. Bragg peaks in (C) and (D) are denoted by red circles. (**D**) $Z(\vec{\mathbf{q}}, E \sim \Delta_1)$ for $p = 0.23$ from (B). No specific broken-symmetry state wave vectors are apparent, whereas the residual dispersive effects of Bogoliubov quasi-particles are seen. (**E**) $\vec{\mathbf{Q}} = 0$ broken C_4-symmetry order parameter $O_N^q(\vec{\mathbf{r}}, E \sim \Delta_1)$ for $p = 0.06$; $\Delta_1 = 124 \pm 1$ meV. This whole field of view is a single color, indicating that long-range $\vec{\mathbf{Q}} = 0$ intra–unit-cell C_4 symmetry breaking exists. (**F**) Intra–unit-cell broken C_4 symmetry $O_N^q(\vec{\mathbf{r}}, E \sim \Delta_1)$ for $p = 0.22$; $\Delta_1 = 28 \pm 1$ meV. Long-range order has been lost, but nanoscale domains of opposite nematicity persist. The dashed circle represents the spatial resolution of the analysis. (**G**) Intensity of incommensurate modulations with wave vector $\vec{\mathbf{q}}_5^*$, $I(\vec{\mathbf{q}}_5^*)$ initially increases upon doping peaking near $p \sim 1/8$, and then diminishes to reach zero at $p \approx 0.19$. (**H**) Squares indicate measured spatial average value of the $\vec{\mathbf{Q}} = 0$ broken C_4 symmetry $|< O_N^q(\vec{\mathbf{r}}, E \sim \Delta_1)>|$, which diminishes steadily with increasing p, to reach zero near $p = 0.19$. Triangles indicate measured standard deviation of O_N^q: $\delta O_N^q(\vec{\mathbf{r}}, E \sim \Delta_1)$.

Next we study the broken-symmetry states by examining $Z(\vec{\mathbf{r}}, E)$ measured simultaneously with the $\vec{\mathbf{k}}$-space data in Fig. 2, but now for $\Delta_0 < |E| < \Delta_1$ (pink regions in Fig. 1B), where Δ_1 is the maximum detectable gap [pseudogap at low p and maximum superconducting gap at high p (35)]. These images exhibit several distinct broken spatial symmetries whose evolution with p we explore. Figure 3A shows $Z(\vec{\mathbf{r}}, E \sim \Delta_1)$ for $p = 0.08$, whereas Fig. 3B shows $Z(\vec{\mathbf{r}}, E \sim \Delta_1)$ for $p = 0.23$, with their Fourier transforms $Z(\vec{\mathbf{q}}, E \sim \Delta_1)$ shown in Fig. 3, C and D, respectively. The former exhibits the widely reported (24–26, 35, 36) quasi-static wave vectors $\vec{\mathbf{q}}_1^*$ and $\vec{\mathbf{q}}_5^*$ of states with local symmetry breaking along with the Bragg peaks (red circle), whereas in the latter, the quasi-static wave vectors $\vec{\mathbf{q}}_1^*$ and $\vec{\mathbf{q}}_5^*$ have disappeared. The $\vec{\mathbf{Q}} = 0$ broken C_4-symmetry states can be detected by using the lattice-phase–resolved nematic order parameter (11)

$$O_N^q(E) = ReZ(\vec{\mathbf{Q}}_y, E) - ReZ(\vec{\mathbf{Q}}_x, E) \quad (3)$$

The $\vec{\mathbf{Q}}_x$ and $\vec{\mathbf{Q}}_y$ are the Bragg vectors after the necessary transformation to nearly perfect lattice periodicity in $Z(\vec{\mathbf{r}}, E)$ so that real and imaginary components of the Bragg amplitudes, $ReZ(\vec{\mathbf{Q}}, E)$ and $ImZ(\vec{\mathbf{Q}}, E)$, are well defined (11, 35). The measured $O_N^q(\vec{\mathbf{r}}, E \sim \Delta_1)$ for $p = 0.06$ and $O_N^q(\vec{\mathbf{r}}, E \sim \Delta_1)$ for $p = 0.23$ are shown in Fig. 3,

E and F, respectively (supplementary text section IV) (38). Here we see that the extensive order in $O_N^q(\vec{\mathbf{r}}, E \sim \Delta_1)$ observed at low p (11) has disappeared at high p, leaving nanoscale domains of opposite nematicity (26) probably nucleated by disorder. The doping dependence of $I(\vec{\mathbf{q}}_5^*)$, the intensity of the $\vec{\mathbf{q}}_5^*$ modulations in $Z(\vec{\mathbf{q}}, E)$, is shown in Fig. 3G (supplementary text section III and figs. S4 and S5) (38), whereas the dependence of the spatially averaged magnitude $|< O_N^q(\vec{\mathbf{r}}, E \sim \Delta_1)>|$ of the $\vec{\mathbf{Q}} = 0$ C_4 breaking is shown in Fig. 3H (supplementary text section IV and figs. S7 and S8) (38). These plots reveal that the more extended $\vec{\mathbf{Q}} = 0$ broken symmetry and the shorter-range ordering tendencies in $\vec{\mathbf{Q}} \neq 0$ modulations (11, 26, 35) disappear near a critical doping $p_c \approx 0.19$.

Figure 4A is a schematic summary of our findings, from Bogoliubov QPI techniques (32, 35, 37), on the dependence of $\vec{\mathbf{k}}$-space electronic structure with increasing p. Fig. 4B shows that the wave vectors $\vec{\mathbf{k}} = \vec{\mathbf{q}}_E/2$ of states at which Bogoliubov QPI disappears (circles) evolve along the $\vec{\mathbf{k}}$-space lines $(\pm 1, 0)\pi/a_0 \rightarrow (0, \pm 1)\pi/a_0$ with increasing p. Concomitantly, the quasi-static wave vectors $\vec{\mathbf{q}}_1^*/2$ and $(2\pi - \vec{\mathbf{q}}_5^*)/2$ of broken-symmetry states also evolve on the same trajectory (squares). Thus, the $\vec{\mathbf{q}}_1^*$ and $\vec{\mathbf{q}}_5^*$ wave vectors of incommensurate (density-wave) modulations evolve with

doping, as shown in Fig. 4C (35). Figure 4D shows the area of $\vec{\mathbf{k}}$-space between the arc and the line $(1, 0)\pi/a_0 \rightarrow (0, 1)\pi/a_0$ (left inset) increasing proportional to hole density p (32, 35); at $p = 0.19$, there is a transition to a diminishing area of electron count as 1-p for the closed-contour FS topology. Finally, we show in Fig. 4, E to G, that the critical point $p_c \approx 0.19$ is associated microscopically with a transition to conventional d-wave Bogoliubov QPI on a complete FS (simulated in Fig. 4E and measured at $p > p_c$ in 4G) from a highly distinct form of scattering (Fig. 4F) of unknown cause (39).

To recapitulate: With increasing hole density, the $\vec{\mathbf{Q}} \neq 0$ modulations (density waves) weaken and disappear at $p_c \approx 0.19$ (Fig. 1A and Fig. 3, A to D and G). Concurrently, the $\vec{\mathbf{Q}} = 0$ broken-symmetry (intra–unit-cell nematic) states become progressively more disordered (13) and reach a zero average value at approximately the same p_c (Fig. 1A and Fig. 3, E to F and H). Simultaneously, the $\vec{\mathbf{k}}$-space topology of coherent Bogoliubov quasi-particles (or the FS supporting their superconducting gap) undergoes an abrupt transition from arcs to closed contours (Figs. 2 and 4 and movie S2) (38). This key transformation of cuprate electronic structure is therefore linked directly with disappearance of electronic symmetry breaking. However, this phenomenology
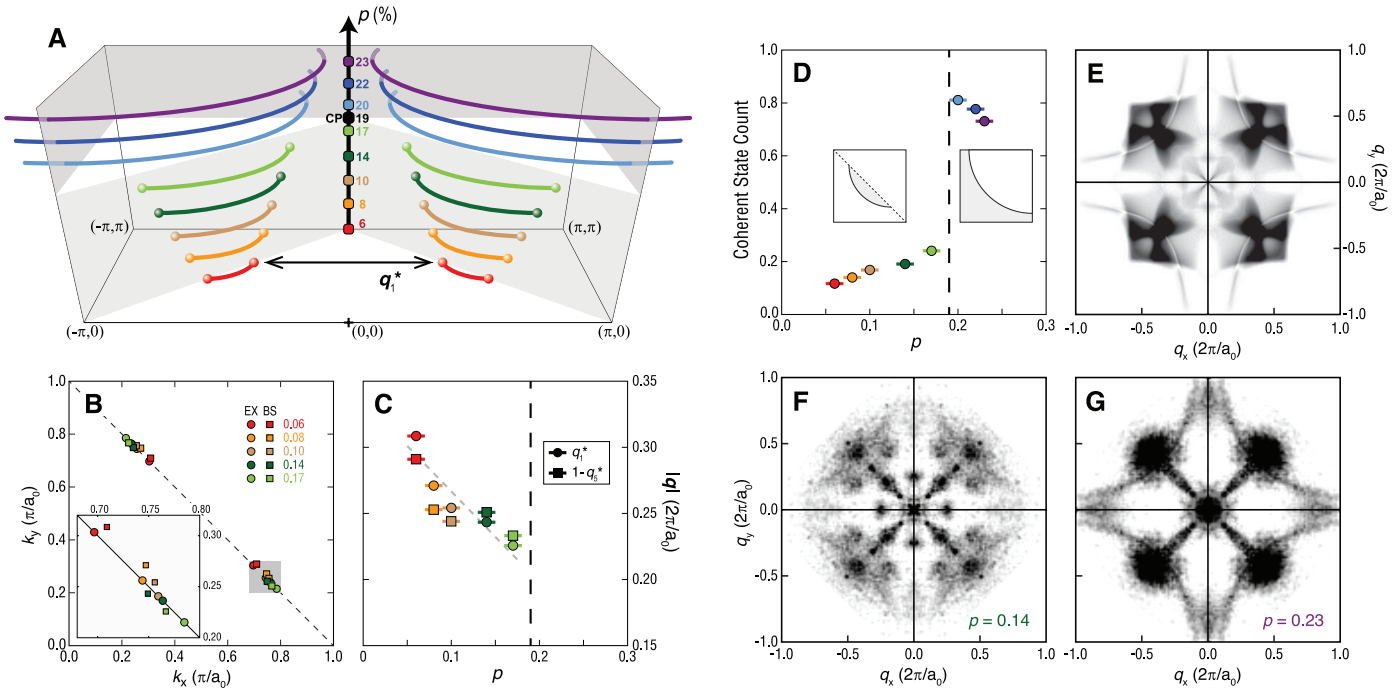
Fig. 4. Interlinked $\vec{\mathbf{k}}$-space structure of Bogoliubov QPI and $\vec{\mathbf{Q}} \neq 0$ symmetry breaking at lines joining $(\pm 1, 0)\pi/a_0$ to $(0, \pm 1)\pi/a_0$. (**A**) Schematic of $\vec{\mathbf{k}}$-space locus of states generating Bogoliubov QPI with increasing hole density in Bi$_2$Sr$_2$CaCu$_2$O$_{8+\delta}$. An abrupt transition occurs at $p \approx 0.19$. (**B**) Measured wave vectors $\vec{\mathbf{k}}$ of states at which Bogoliubov QPI disappears $\vec{\mathbf{q}}_E/2$ (circles), and those of the quasi-static broken-symmetry modulations with $\vec{\mathbf{q}}_1^*/2$ and $(2\pi - \vec{\mathbf{q}}_5^*)/2$ (squares). (**C**) Measured doping dependence of wave vectors of incommensurate conductance modulations (density waves) $\vec{\mathbf{q}}_1^*$ and $\vec{\mathbf{q}}_5^*$ derived from (B) (*35*). The vertical dashed line indicates p_c. (**D**) The $\vec{\mathbf{k}}$-space area between the arc and the line joining $(\pm 1, 0)\pi/a_0$ to $(0, \pm 1)\pi/a_0$ is proportional to p. With the appearance of the closed FS at $p \approx 0.19$, there is a transition to a diminishing area of electron count $1 - p$. Insets, $\vec{\mathbf{k}}$-space areas used. (**E**) T-matrix scattering interference simulation for $\Lambda(\vec{\mathbf{q}})$ for a complete FS and d-wave gap with conventional (time-reversal preserving) scattering. (**F**) Measured $\Lambda(\vec{\mathbf{q}})$ for $p = 0.14$ ($\Delta_0 = 34 \pm 1$meV) is in sharp contrast to the simulation result in (E). (**G**) For $p = 0.23$, $\Lambda(\vec{\mathbf{q}})$ conforms closely to the conventional d-wave Bogoliubov scattering scheme, as anticipated in (E).

also exhibits many peculiar components unexpected within a simple FS reconstruction scenario. First, the coevolution and contiguous disappearance at p_c of the signatures of two distinct broken symmetries (Figs. 1A and 3) reinforce the deductions that they are microscopically closely related (*11, 26, 35, 36, 40*). Second, because the $\vec{\mathbf{Q}} \neq 0$ modulations exhibit wave vectors generated by scattering regions (hot spots) moving along the $\vec{\mathbf{k}}$-space lines $(\pm 1, 0)\pi/a_0 \rightarrow (0, \pm 1)\pi/a_0$ (Fig. 4, A to C) (*32, 35*), FS nesting provides an inadequate explanation for the cuprate density waves. Third, the abrupt $\vec{\mathbf{k}}$-space topology change at p_c (Fig. 2E and Fig. 4, A, F, and G) exhibits characteristics more reminiscent of an antinodal coherence recovery transition (*41*) than of a conventional band reorganization. Fourth, because the disappearance of the pseudogap is associated axiomatically with the reappearance of coherent antinodal states, and because the latter is precisely what occurs at p_c (Figs. 2E and 4A), the pseudogap (*1–3*) and the electronic symmetry breaking (*5–25*) must be intimately linked (Fig. 1A). Finally, as neither long-range $\vec{\mathbf{Q}} \neq 0$ order nor any associated quantum critical point can exist with quenched disorder (*40*), a nematic critical point, at which the electronic symmetry breaking between the two oxygen

sites within the CuO$_2$ unit cell (*11, 26, 35, 36*) disappears, seems most consistent with our observations.

References and Notes

1. J. Orenstein, A. J. Millis, *Science* **288**, 468–474 (2000).
2. M. R. Norman, D. Pines, C. Kallin, *Adv. Phys.* **54**, 715–733 (2005).
3. T. Timusk, B. Statt, *Rep. Prog. Phys.* **62**, 61–122 (1999).
4. S. A. Kivelson, E. Fradkin, V. J. Emery, *Nature* **393**, 550–553 (1998).
5. A. Kaminski *et al.*, *Nature* **416**, 610–613 (2002).
6. B. Fauqué *et al.*, *Phys. Rev. Lett.* **96**, 197001 (2006).
7. H. A. Mook, Y. Sidis, B. Fauqué, V. Balédent, P. Bourges, *Phys. Rev. B* **78**, 020506 (2008).
8. Y. Li *et al.*, *Nature* **455**, 372–375 (2008).
9. J. Xia *et al.*, *Phys. Rev. Lett.* **100**, 127002 (2008).
10. R.-H. He *et al.*, *Science* **331**, 1579–1583 (2011).
11. M. J. Lawler *et al.*, *Nature* **466**, 347–351 (2010).
12. Y. Li *et al.*, *Phys. Rev. B* **84**, 224508 (2011).
13. S. De Almeida-Didry *et al.*, *Phys. Rev. B* **86**, 020504(R) (2012).
14. A. Shekhter *et al.*, *Nature* **498**, 75–77 (2013).
15. J. M. Tranquada, B. J. Sternlieb, J. D. Axe, Y. Nakamura, S. Uchida, *Nature* **375**, 561–563 (1995).
16. M. Hücker *et al.*, *Phys. Rev. B* **83**, 104506 (2011).
17. Y.-J. Kim, G. Gu, T. Gog, D. Casa, *Phys. Rev. B* **77**, 064520 (2008).
18. J. Chang *et al.*, *Nat. Phys.* **8**, 871–876 (2012).
19. G. Ghiringhelli *et al.*, *Science* **337**, 821–825 (2012).
20. A. J. Achkar *et al.*, *Phys. Rev. Lett.* **109**, 167001 (2012).
21. D. H. Torchinsky, F. Mahmood, A. T. Bollinger, I. Božović, N. Gedik, *Nat. Mater.* **12**, 387–391 (2013).
22. E. Blackburn *et al.*, *Phys. Rev. Lett.* **110**, 137004 (2013).
23. J. P. Hinton *et al.*, *Phys. Rev. B* **88**, 060508(R) (2013).
24. R. Comin *et al.*, *Science* **343**, 390–392 (2014).
25. E. H. da Silva Neto *et al.*, *Science* **343**, 393–396 (2014).
26. A. Mesaros *et al.*, *Science* **333**, 426–430 (2011).
27. J. L. Tallon, J. W. Loram, *Physica C* **349**, 53–68 (2001).
28. A. J. Millis, M. R. Norman, *Phys. Rev. B* **76**, 220503(R) (2007).
29. A. G. Loeser *et al.*, *Science* **273**, 325–329 (1996).
30. M. R. Norman *et al.*, *Nature* **392**, 157–160 (1998).
31. K. M. Shen *et al.*, *Science* **307**, 901–904 (2005).
32. Y. Kohsaka *et al.*, *Nature* **454**, 1072–1078 (2008).
33. M. Platé *et al.*, *Phys. Rev. Lett.* **95**, 077001 (2005).
34. B. Vignolle *et al.*, *Nature* **455**, 952–955 (2008).
35. K. Fujita *et al.*, *J. Phys. Soc. Jpn.* **81**, 011005 (2012).
36. Y. Kohsaka *et al.*, *Science* **315**, 1380–1385 (2007).
37. Y. He *et al.*, *Science* **344**, 608–611 (2014).
38. Materials and methods are available as supplementary materials on *Science* Online.
39. E.-A. Kim, M. J. Lawler, *Phys. Rev. B* **81**, 132501 (2010).
40. L. Nie, G. Tarjus, S. A. Kivelson, http://arxiv.org/abs/1311.5580
41. U. Chatterjee *et al.*, *Proc. Natl. Acad. Sci. U.S.A.* **108**, 9346–9349 (2011).

Direct, Nonoxidative Conversion of Methane to Ethylene, Aromatics, and Hydrogen

Xiaoguang Guo,[1] Guangzong Fang,[1] Gang Li,[2,3] Hao Ma,[1] Hongjun Fan,[2] Liang Yu,[1] Chao Ma,[4] Xing Wu,[5] Dehui Deng,[1] Mingming Wei,[1] Dali Tan,[1] Rui Si,[6] Shuo Zhang,[6] Jianqi Li,[4] Litao Sun,[5] Zichao Tang,[2] Xiulian Pan,[1] Xinhe Bao[1]*

The efficient use of natural gas will require catalysts that can activate the first C–H bond of methane while suppressing complete dehydrogenation and avoiding overoxidation. We report that single iron sites embedded in a silica matrix enable direct, nonoxidative conversion of methane, exclusively to ethylene and aromatics. The reaction is initiated by catalytic generation of methyl radicals, followed by a series of gas-phase reactions. The absence of adjacent iron sites prevents catalytic C-C coupling, further oligomerization, and hence, coke deposition. At 1363 kelvin, methane conversion reached a maximum at 48.1% and ethylene selectivity peaked at 48.4%, whereas the total hydrocarbon selectivity exceeded 99%, representing an atom-economical transformation process of methane. The lattice-confined single iron sites delivered stable performance, with no deactivation observed during a 60-hour test.

The challenge of converting natural gas into transportable fuels and chemicals (*1*) has been spurred by several emerging industrial trends, including rapidly rising demand for H$_2$ (for upgrading lower-quality oils) and a global shortage of aromatics caused by shifting refinery targets toward gasoline. Light olefins, which are key chemical feedstocks, are currently made from methanol, which itself is made through multistage catalytic transformations via syngas (a mixture of H$_2$ and CO) (*2*, *3*), although there is also ongoing research to convert syngas directly to light olefins (*4*, *5*). However, in all such approaches, either CO or H$_2$ is needed to remove oxygen from CO, resulting in a carbon-atom utilization efficiency below 50%. Despite their low efficiency, high capital and production costs, and enormous CO$_2$ emissions,

syngas routes dominate current and near-term industrial practices for natural gas conversion (*6*, *7*).

Direct conversion of CH$_4$ is potentially more economical and environmentally friendly but is challenging because CH$_4$ exhibits high C–H bond strength (434 kJ/mol), negligible electron affinity, large ionization energy, and low polarizability (*8*). In the pioneering work of Keller and Bhasin in the early 1980s, CH$_4$ was activated with the assistance of oxygen (*9*). This finding initiated a worldwide research surge to explore the high-temperature (>1073 K) oxidative coupling of methane (OCM) to C$_2$ hydrocarbons (*10*, *11*). Hundreds of catalytic materials have since been synthesized and tested, principally during the 1990s, as well as in recent years. Unfortunately, the presence of O$_2$ leads irreversibly to overoxidation, resulting in a large amount of the thermodynamically stable end-products CO$_2$ and H$_2$O. Thus, the carbon utilization efficiency of OCM remains relatively low (*12*, *13*). Slow progress in discovering new catalysts to circumvent this problem has hindered further development, and no economically viable process has been put into practice so far.

In a recent report, elemental sulfur was used as a softer oxidant than O$_2$ (*14*): For a 5% CH$_4$/Ar mixture at 1323 K, the best catalyst, PdS/ZrO$_2$, gave a CH$_4$ conversion of ~16% and ethylene selectivity near 20%, albeit at the expense of the by-products CS$_2$ and H$_2$S (*14*). In contrast, the bifunctional catalysts based on Mo/zeolites catalyze CH$_4$ conversion to aromatics (benzene and

naphthalene) nonoxidatively, thereby avoiding CO$_2$ formation (*15–18*). CH$_4$ is activated on the metal sites forming CH$_x$ species, which dimerize to C$_2$H$_y$. Subsequent oligomerization on the acidic sites located inside the zeolite pores yields benzene and naphthalene, as well as copious amounts of coke (*19–21*). Commercial prospects for this process are further hampered by the instability of zeolites at the very high reaction temperatures.

To achieve direct conversion of CH$_4$ efficiently, the challenges lie in cleaving the first C–H bond while suppressing further catalytic dehydrogenation, avoiding both CO$_2$ generation and coke deposition. We report that these conditions can be met using lattice-confined single iron sites embedded in a silica matrix. These sites activate CH$_4$ in the absence of oxidants, generating methyl radicals, which desorb from the catalyst surface and then undergo a series of gas-phase reactions to yield ethylene, benzene, and naphthalene as the only products (with ethylene dominating at short space-times for a selectivity of ~52.7% at 1293 K). A methane conversion as high as 48.1% is achieved at 1363 K.

The catalysts were obtained by fusing ferrous metasilicate with SiO$_2$ at 1973 K in air and from commercial quartz, followed by leaching with aqueous HNO$_3$ and drying at 353 K (*22*). The resulting catalyst was designated 0.5% Fe©SiO$_2$ (© denotes confinement and here represents a catalyst characterized by the lattice-confined single iron sites embedded within a silica matrix). It contained 0.5 weight percent (wt %) Fe and had a Brunauer–Emmett–Teller surface area of <1 m^2/g. The catalyst was activated in a fixed-bed microreactor in the reaction atmosphere [90 volume percent (vol %) CH$_4$/N$_2$] at 1173 K. The effluent was analyzed by online gas chromatography (GC). At 1223 K, CH$_4$ conversion was 8.1% (Fig. 1A) and increased with temperature, exceeding 48.1% at 1363 K (Fig. 1B). Only ethylene, benzene, and naphthalene were produced; neither coke nor CO$_2$ was detected, despite the relatively high reaction temperature. A single-pass yield of 48% hydrocarbons is achieved at 1363 K and 21.4 liters per gram of catalyst (gcat) per hour. Selectivities vary from 40.9 to 52.1% for ethylene, 21.0 to 29.1% for benzene, and 23.6 to 38.2% for naphthalene, over the investigated temperature range (1223 to 1363 K).

By comparison, a blank experiment (an empty reactor with no catalyst) under the same conditions showed a CH$_4$ conversion of only 2.5%, and 95% of the product was coke (Fig. 1A). A test with unmodified SiO$_2$ as the catalyst yielded virtually

[1]State Key Laboratory of Catalysis, Dalian Institute of Chemical Physics, Chinese Academy of Sciences, Dalian 116023, People's Republic of China. [2]State Key Laboratory of Molecular Reaction Dynamics, Dalian Institute of Chemical Physics, Chinese Academy of Sciences, Dalian 116023, People's Republic of China. [3]State Key Laboratory of Fine Chemicals, Institute of Coal Chemical Engineering, School of Chemical Engineering, Dalian University of Technology, Dalian 116012, People's Republic of China. [4]Beijing National Laboratory for Condensed Matter Physics, Institute of Physics, Chinese Academy of Sciences, Beijing 100190, People's Republic of China. [5]Nano-Pico Center, Key Laboratory of Micro-Electro-Mechanical System (MEMS) of Ministry of Education, Southeast University, Nanjing 210096, People's Republic of China. [6]Shanghai Synchrotron Radiation Facility, Shanghai Institute of Applied Physics, Chinese Academy of Sciences, Shanghai 201204, People's Republic of China.

*Corresponding author. E-mail: xhbao@dicp.ac.cn